ACS APPLIED ELECTRONIC MATERIALS

pubs.acs.org/acsaelm

Article

Impact of Indium Doping in Lead-Free $(CH_3NH_3)_3Bi_{2-x}In_xI_9$ Perovskite Photovoltaics for Indoor and Outdoor Light Harvesting

Ramesh Kumar, Hairui Liu, Seyed Ali Nabavi, Moses S. Anyebe, Suhas Mahesh, Henry Snaith, Monojit Bag, and Sagar M. Jain*

Cite This: ACS Appl. Electron. Mater. 2024, 6, 8360−8368

Read Online

ACCESS | Metrics & More | Article Recommendations | Supporting Information

ABSTRACT: Hybrid halide perovskites (HHPs) have revolutionized the field of solar cells due to their low cost, solution-processable synthesis, and exceptional device performance. Although lead (Pb)-based perovskites are currently the most efficient, their application in indoor photovoltaics and wearable electronics is limited by lead's toxicity. This has intensified the search for Pb-free alternatives, particularly for use in portable electronic devices. In this study, we utilized a vapor-assisted solution process to systematically engineer the composition of bismuth-based perovskite-inspired materials (PIMs) through indium doping, forming homogeneous and pinhole-free $(CH_3NH_3)_3Bi_{2-x}In_xI_9$ (Bi−In) films. These bimetallic Bi−In perovskites exhibit enhanced properties, including high recombination resistance, reduced low-frequency capacitance, lower defect density, and minimal microstrain. Electrochemical impedance spectroscopy (EIS) shows significantly reduced ion migration in Bi−In compositions compared with pure bismuth-based counterparts. The optimized Bi−In-based solar cells achieved a power conversion efficiency (PCE) of 2.5% under outdoor illumination and 5.9% under indoor lighting, showcasing their potential as promising lead-free alternatives for photovoltaic applications.

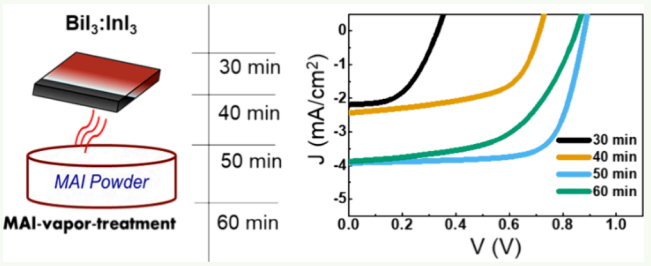

KEYWORDS: *lead-free perovskites, nontoxicity, environmentally friendly, portable electronics, solar cells*

1. INTRODUCTION

Hybrid halide perovskites have attracted great attention from the scientific community due to their exceptional optoelectronic properties,[1−5] low-cost solution-processed fabrication method,[6−10] and, most importantly, flexibility to fine-tune the band gap that enables them to use over a wide range of applications.[11−13] In the past decade, the power conversion efficiency of lead halide perovskite solar cells has skyrocketed.[14−16] However, the toxicity and intrinsic instability of lead halide perovskite solar cells are still a bottleneck for their commercialization and eco-friendly environment. In this context, the scientific community recently started looking for lead-free materials for photovoltaic devices for indoor light harvesting.[17−21] For instance, the power conversion efficiency (PCE) of tin (Sn)-based perovskite photovoltaics has already reached 15%.[22,23] However, Sn^{2+} rapidly oxidizes to Sn^{4+} when subjected to an ambient environment that results in poor stability during device operation.[24]

Therefore, the exploration of less toxic yet stable perovskite-inspired materials for indoor photovoltaics (IPVs) emerges as a crucial and highly challenging research endeavor. Recently, there has been a search for alternative antimony(III) Sb^{3+} and bismuth(III) Bi^{3+}-based materials to be employed in perovskite photovoltaics.[25−29] To date, the highest efficiency reported using Bi-based solar cells reached around 3.5%.[8,30,31] Despite their poor performance, they possess the future potential for improvement in indoor energy applications because of their suitable optoelectronic properties and high chemical stability.[32] The $A_3Bi_2X_9$ [A = $CH_3NH_3^+$ (MA), $CH(NH_2)^{2+}$ (FA) or Cs; X = I, Br, Cl] class of low-dimensional perovskite materials has been much investigated as an absorber layer for solar cell applications.[33] There have been very few reports on this class of materials for PV applications; however, they still depict much inferior certified PCE at the current stage. It mainly accounts for the poor-quality film morphology, low electronic conductivity, and high optical band gap. In this direction, we have reported a vapor-assisted solution process method by exposing BiI_3 films to CH_3NH_3I (MAI) vapors and forming good-quality Bi-based perovskite films.[8] However, residual unreacted MAI was observed in the thin films. To further improve the film quality, it is crucial to reduce the formation of excess MAI in the vapor-assisted method. Another approach to enhancing the efficiency of $A_3B_2X_9$-based solar cells is

Received: September 4, 2024
Revised: October 9, 2024
Accepted: October 10, 2024
Published: October 17, 2024

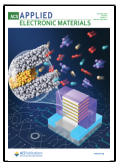

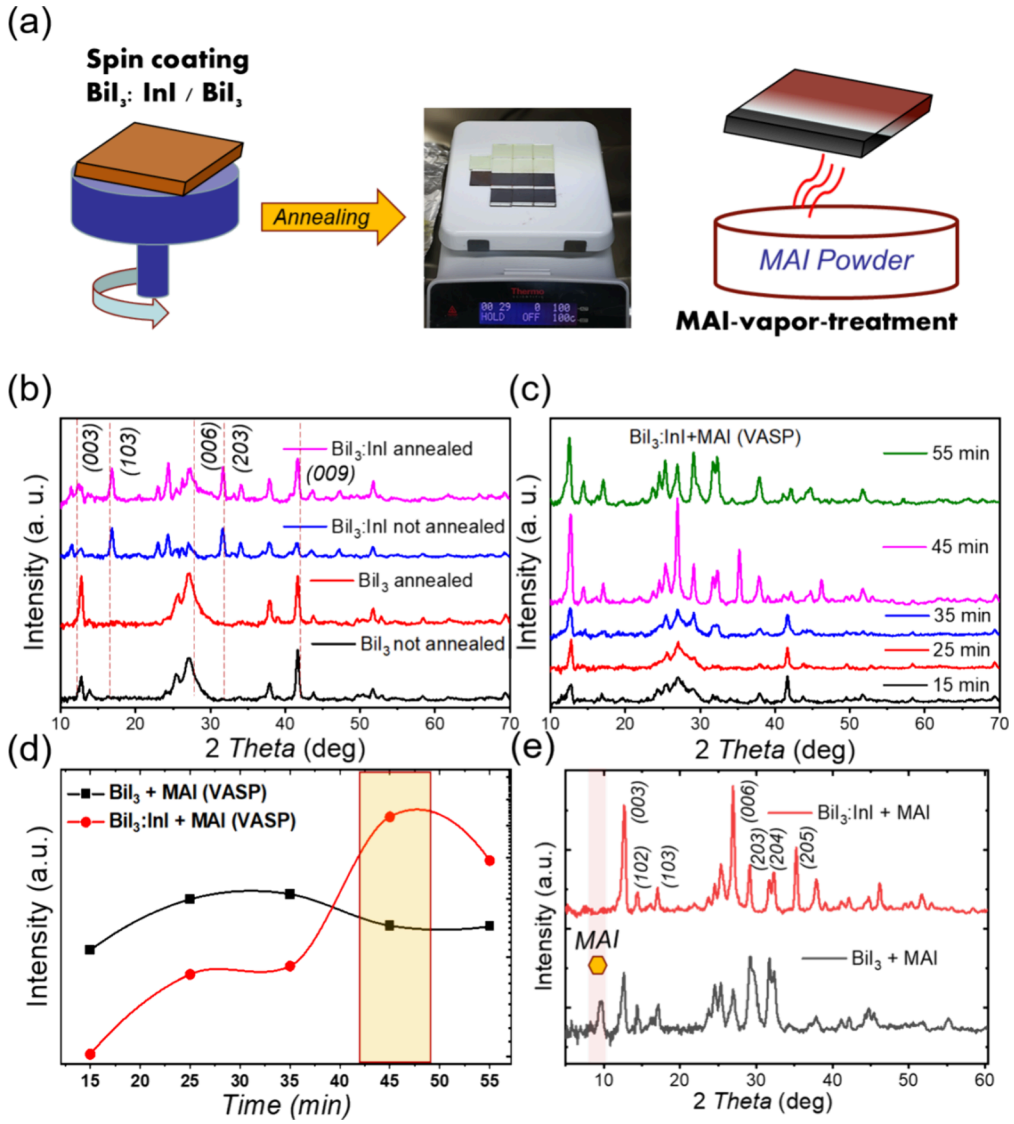

Figure 1. (a) Schematic illustration of preparation of compact and uniform perovskite thin films via a vapor-assisted solution process method. X-ray diffraction patterns of (b) spin-coated BiI_3 and BiI_3:InI_3 thin films and (c) vapor-assisted BiI_3:InI_3 + MAI thin films at different reaction times. (d) Variation of the (003) peak intensity with different reaction times for pristine and $(CH_3NH_3)_3Bi_{2-x}In_xI_9$ perovskite thin films. (e) XRD diffraction patterns of both pristine and doped $(CH_3NH_3)_3Bi_2I_9$ perovskite thin films at 45 min.

compositional engineering. Recently, Paola et al. reported the development of triple-cation-based Sb perovskites (CsMAFA-Sb) for indoor photovoltaic applications. Through effective compositional engineering strategies, they achieved a PCE of 2.47% under standard illumination (1 Sun) and 6.4% under 1000 lx lighting conditions.[34]

Herein, we employed InI_3 in BiI_3 films to fabricate high-quality Bi−In-based perovskite-inspired materials (PIMs). This approach results in smooth, compact films with larger grain sizes, enhancing the efficiency of the Pb-free perovskite solar cells. The incorporation of InI_3 into BiI_3 resulted in the formation of good quality thin films of PIMs. InI_3 helps to control the crystallization process and growth rate of the perovskite crystals, leading to smoother, more uniform films. It also aids in managing the reaction with MAI vapor, reducing the presence of excess MAI, contributing to the formation of high-quality PIMs, and playing a role in repairing interstitial iodide vacancies. The In^{3+} incorporation at the B site also acts as a passivating agent for surface sites and improves the ambient and operational stability.[35] Also, in the vapor-assisted method, the reaction time between BiI_3 and MAI plays a very crucial role in yielding a homogeneous nucleation process, allowing one to fine-tune the crystallization process. We have performed several characterization techniques such as X-ray diffraction (XRD), scanning electron microscopy (SEM), Fourier transform infrared spectroscopy (FTIR), Raman spectroscopy, and absorption spectroscopy to probe the structural, top-view surface morphological, and chemical constituents of pristine and In^{3+}-incorporated $(CH_3NH_3)_3Bi_2I_9$ films prepared by reaction of MAI vapor at different reaction times. We further fabricated an n−i−p mesoporous device structure of glass/fluorine-doped tin oxide (FTO)/mesoscopic TiO_2/$(CH_3NH_3)_3Bi_2I_9$/Spiro-OMeTAD/Ag, and (FTO)/m-TiO_2/$(CH_3NH_3)_3Bi_{2-x}In_xI_9$/Spiro-OMeTAD/Ag. The maximum PCE of 2.55% was obtained for the solar cells made from the Bi−In absorber layer with a reaction time of 45 min. We further performed electrical measurements to get insight into trap density, recombination, and ion dynamics. Overall, this

https://doi.org/10.1021/acsaelm.4c01576
ACS Appl. Electron. Mater. 2024, 6, 8360−8368

research emphasizes the critical role of reaction time management in the vapor-assisted method and the strategic engineering of B-site composition.

2. EXPERIMENTAL METHODS

Materials Used. Bismuth(III) iodide (BiI_3: 99.99%), *N*,*N*-dimethylformamide (DMF), dimethyl sulfoxide (DMSO: super dehydrated), indium(III) iodide (BiI_3: 99.99%), Spiro-OMeTAD, and methylammonium iodide (CH_3NH_3I: MAI: 99.99%) were purchased from Sigma-Aldrich.

Preparation of Bi-Based Perovskite Thin Films. We have used our previously reported vapor-assisted solution process to prepare bismuth-based perovskite thin films for photovoltaic devices.[8] In this method, first, BiI_3 was dissolved in a cosolvent of DMF and DMSO (DMF:DMSO = 3:2) at room temperature (RT) in a vial with constant stirring for 2 h (see Figure S1). This precursor solution of BiI_3 was spin-coated at 4000 rpm on a TiO_2-coated FTO substrate according to our previously reported method. For In^{3+}-doped perovskites, we have incorporated the InI_3 precursor solutions (1 v/v %) into the BiI_3 solution (10.1 μL of InI_3 into 1 mL of BiI_3). The BiI_3 and BiI_3:InI_3 spin-coated samples were annealed at 100 °C for 20 and 40 min, respectively. After cooling down, the annealed spin-coated films were placed in a glass Petri dish with MAI powder placed surrounding the films for vapor treatment, as shown in Figures S2 and S3. The Petri dish was heated at 150° C for different reaction times of 15, 25, 35, 45, and 55 min.

Fabrication of Devices. FTO glass substrates were etched with 2 M HCl, and zinc powder was washed with IPA, acetone, and clean water and dried before use. We have spin-coated TiO_2 solution on the etched FTO substrate at 3000 rpm for 30 s and then sintered it for 450 °C for 1 h to form a compact morphology. The mesoporous TiO_2 layer for electron transport was prepared according to the previously reported method (spin coating a diluted TiO_2 paste at 4000 rpm for 30 s, followed by annealing at 550 C for 30 min on a hot plate). After cooling down the sintered TiO_2 substrates, we coated bismuth perovskite thin films by VASP, as discussed above. For the hole transport layer (HTL), we spin-coated Spiro-OMeTAD solution at 2000 rpm for 30 s and annealed it at 50 °C for 60 s. Finally, the Ag metal electrode was thermally deposited as an anode in 2×10^{-6} mbar vacuum pressure to complete the device configuration.

3. RESULTS AND DISCUSSION

The surface morphology of the bismuth-based perovskite-inspired material (PIM) films is crucial for the fabrication of efficient, lead-free PV devices. Therefore, pristine or reference $(CH_3NH_3)_3Bi_2I_9$ (Bi) and InI_3-incorporated $(CH_3NH_3)_3Bi_{2-x}In_xI_9$ (Bi−In) perovskite thin films were fabricated using the vapor-assisted solution process method. In this method, crystal growth can be controlled via in situ reaction time between the as-deposited film of BiI_3 and CH_3NH_3I (MAI) vapor treatment, as shown in Figure 1a. The underlying crystallization kinetics of Bi-based perovskite thin-film fabrication were monitored as a function of reaction time by using a series of characterizations such as XRD, FESEM, FTIR, and Raman spectroscopy. In this method, we first spin-coated BiI_3 and annealed it for a few minutes, following our previous work.[8] For the Bi−In perovskites, InI_3 was added to the BiI_3 precursor solution. The incorporation of InI_3 could help to control the crystallization process and the growth rate of the perovskite crystals, resulting in a more uniform film. Subsequently, the BiI_3- and BiI_3:InI_3-coated films were exposed to MAI vapor for different time scales to form $(CH_3NH_3)_3Bi_2I_9$ and $(CH_3NH_3)_3Bi_{2-x}In_xI_9$, as shown in Figure 1.

Figure 1b depicts the XRD patterns of BiI_3 and BiI_3:InI_3 spin-coated films before and after annealing. The diffraction angles at 12.5, 14.6, 17.0, 25.3, 26.9, and 29° correspond to (003), (102), (103), (006), (203), (204), and (205) reflection planes, respectively, which indicates the formation of a good-quality hexagonal phase of both thin films. For BiI_3:InI_3 thin films, two additional peaks appeared corresponding to (103) and (203) reflection planes at 16 and 32°, respectively, indicating the formation of bimetallic Bi−In perovskite. As expected, the intensity of the (003) and (006) planes increased from preannealed to postannealed samples of BiI_3 and BiI_3:InI_3 thin films, indicating increased crystallization of respective metal halides. On MAI vapor treatment on both thin films at different reaction times such as 15, 25, 35, 45, and 55 min, there is a color change from dark brown to light red, suggesting conversion of the BiI_3 phase to the $(CH_3NH_3)_3Bi_2I_9$-based perovskite phase, as shown in the Supporting Information (see Figures S2 and S3). The XRD pattern of both Bi and Bi−In thin films shows a hexagonal phase with a (P63/mmc) space group. The lattice constants of the corresponding hexagonal phase of the pristine and In^{3+}-doped Bi-based perovskites are 5.89 and 5.82 Å, respectively.[1] The reduction in the lattice constant of the hexagonal system of In^{3+}-doped perovskite films reveals a stronger interaction between the MA-site cation and the I-site halide. We have also observed a prominent reflection peak at 9.18° in the pristine thin films,[26] indicating the presence of excess MAI. This peak is expected as a result of the reaction between BiI_3 and nonstoichiometric excess MAI. However, we did not observe any reflection peaks associated with excess MAI in $(CH_3NH_3)_3Bi_{2-x}In_xI_9$, suggesting that the precursor materials (BiI_3:InI_3+MAI) have been fully converted into the pure $(CH_3NH_3)_3In_xBi_{x-1}I_9$ phase. It is evident that In^{3+} helps to manage excess MAI during the vapor treatment, facilitating precise composition control. This results in the formation of homogeneous and good-quality Bi−In-based thin films. Therefore, the incorporation of InI_3 into BiI_3 could accelerate the nucleation process during the reaction with MAI, leading to the more efficient formation of thin films. The XRD patterns of Bi and Bi−In thin films at different reaction times are given in Figure 1d and Figure S4. Furthermore, to investigate the structural changes due to excess MAI, we quantified the lattice strain from the XRD patterns of both samples using the Williamson−Hall (W−H) plot.[36]

$$4\epsilon \sin\theta = \beta \cos\theta + \frac{0.9\lambda}{D} \quad (1)$$

where ϵ is an induced microstrain in the sample, β is the full-width at half-maximum (FWHM) of diffraction plane peaks, θ is the diffraction angle, D *is* the crystallite size, λ (1.546 Å) is the incident X-ray wavelength for Cu Kα radiation, and θ is the position of the diffraction peak. The W−H plots of pure Bi- and Bi−In-based perovskites are given in the Supporting Information (Figure S5a,c). The lattice microstrains were calculated to be 0.0165 and 0.0137 for the Bi and Bi−In perovskites, respectively. Remarkably, the microstrain in the pure Bi lattice was observed to be higher, which can be attributed to the lattice deformation caused by the excess, unreacted MAI.[37] Lead-based perovskites typically exhibit microstrain values in the range of 0.002 to 0.019 ± 0.001.[38] Therefore, the microstrain values of 0.0165 and 0.0137 for the Bi and Bi−In perovskites are within a comparable range. The Urbach energy is calculated from the UV absorption spectrum (see Figure S5b,c) to check the energetic disorder in the band edges of both semiconductor materials according to the following equation:

https://doi.org/10.1021/acsaelm.4c01576
ACS Appl. Electron. Mater. 2024, 6, 8360−8368

$$\ln(\alpha) = \ln(\alpha_0) + \frac{h\nu - E_g}{E_u} \quad (2)$$

Here, α is the absorption coefficient, $h\nu$ is the energy of the incident photon, E_g is the optical band gap, and E_U is known as the Urbach energy. The Urbach energies for the pristine and In^{3+}-doped thin films are 0.580 and 0.476 eV, respectively. This indicates that the excess unreacted MAI in pristine structures introduces significantly more defects and deformations than that in In^{3+}-incorporated structures. However, the Urbach energy is very low in Pb-based perovskite thin films.[2] For surface morphology, FESEM images of the spin-coated BiI_3 and BiI_3:InI_3 thin films and these thin films after MAI vapor treatment (MAI+BiI_3, MAI+BiI_3:InI_3) are reported (Figure 2). It is observed that the introduction of MAI vapors significantly affected the surface morphology of both films. Also, the top-view surface morphology of the Bi−In films shows the formation of a compact pinhole-free and larger grain-sized morphology throughout the film as compared to pristine Bi thin films. Therefore, incorporating In^{3+} into BiI_3 thin films plays a crucial role in controlling the crystallization process of Bi-based perovskite thin films. The top-view surface morphology and EDX elemental mapping of annealed and non-annealed BiI_3 and BiI_3:InI_3 thin films and films after exposure to $MAI_{(v)}$ for 15, 25, 35, 45, and 55 min of reaction time are given in the Supporting Information (see Figures S6 and S7). In addition, the XPS spectra of the Bi−In composition is given in the Supporting Information (Figure S8) showing Bi^{3+}, 4d and In^{3+}, 3d core levels, confirming the formation of the Bi−In metallic phase.

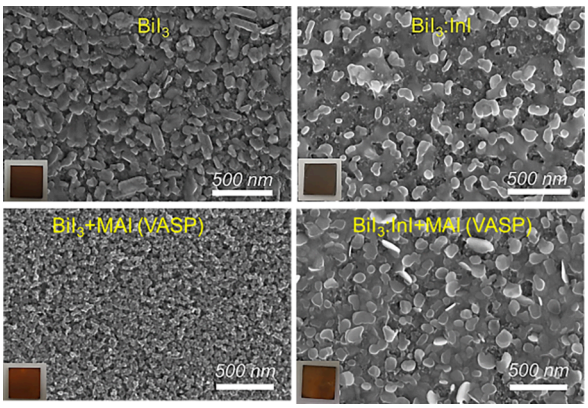

Figure 2. Surface morphology of spin-coated BiI_3 and BiI_3:InI_3 thin films and these thin films after MAI vapor treatment (MAI+BiI_3, MAI +BiI_3:InI_3) at reaction times of 35 and 45 min.

To provide insight into the chemical constituents as well as crystalline and X-ray amorphous bismuth perovskite-like phases of both films, we performed resonance Raman spectroscopy and FTIR on pristine and In^{3+}-doped films. Figure 3a,b presents the FTIR spectra with the characteristic vibrational modes of Bi and Bi−In thin films deposited on glass substrates. The high-frequency vibrational modes between 3250 and 2950 cm^{-1} are associated with the N−H stretching vibrations due to the NH_3^+ group of the MA^+ cation. The doublet modes of N−H vibrations (υ_1, υ_2) have been attributed to asymmetric and symmetric N−H stretching. The characteristic peak at υ_3 = 2950 cm^{-1} exhibits C−H stretching vibrations in both films. In addition, vibrational peaks at lower wavenumbers between 800 and 1800 cm^{-1} correspond to the bending and rocking modes of C−H. FTIR characterization of both thin films was performed in an ambient environment to study the moisture stability of the Bi and Bi−In perovskite films. The distinct peak at around 3600 cm^{-1} in pristine thin films is related to the O−H stretching vibrations.

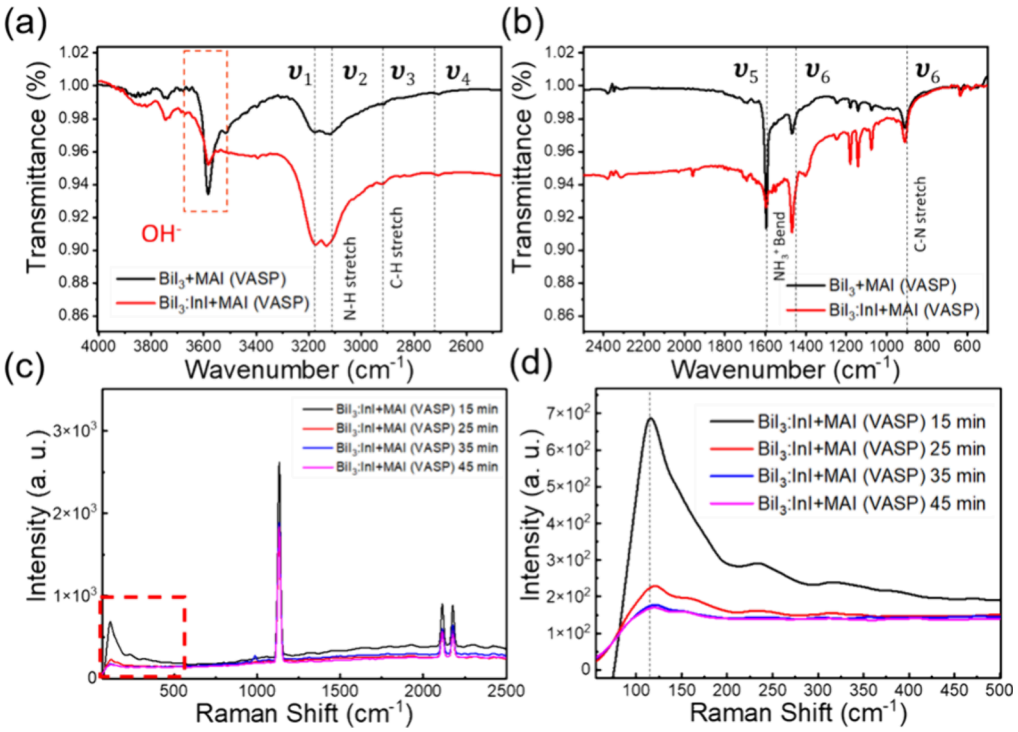

Figure 3. FTIR spectra of MAI+BiI_3 and MAI+BiI_3:InI_3 absorber layers at (a) low frequency and (b) high frequency. (c, d) Raman spectra of the MAI+BiI_3:InI_3 absorber layer at different reaction times at low and high vibrational frequencies.

https://doi.org/10.1021/acsaelm.4c01576
ACS Appl. Electron. Mater. 2024, 6, 8360−8368

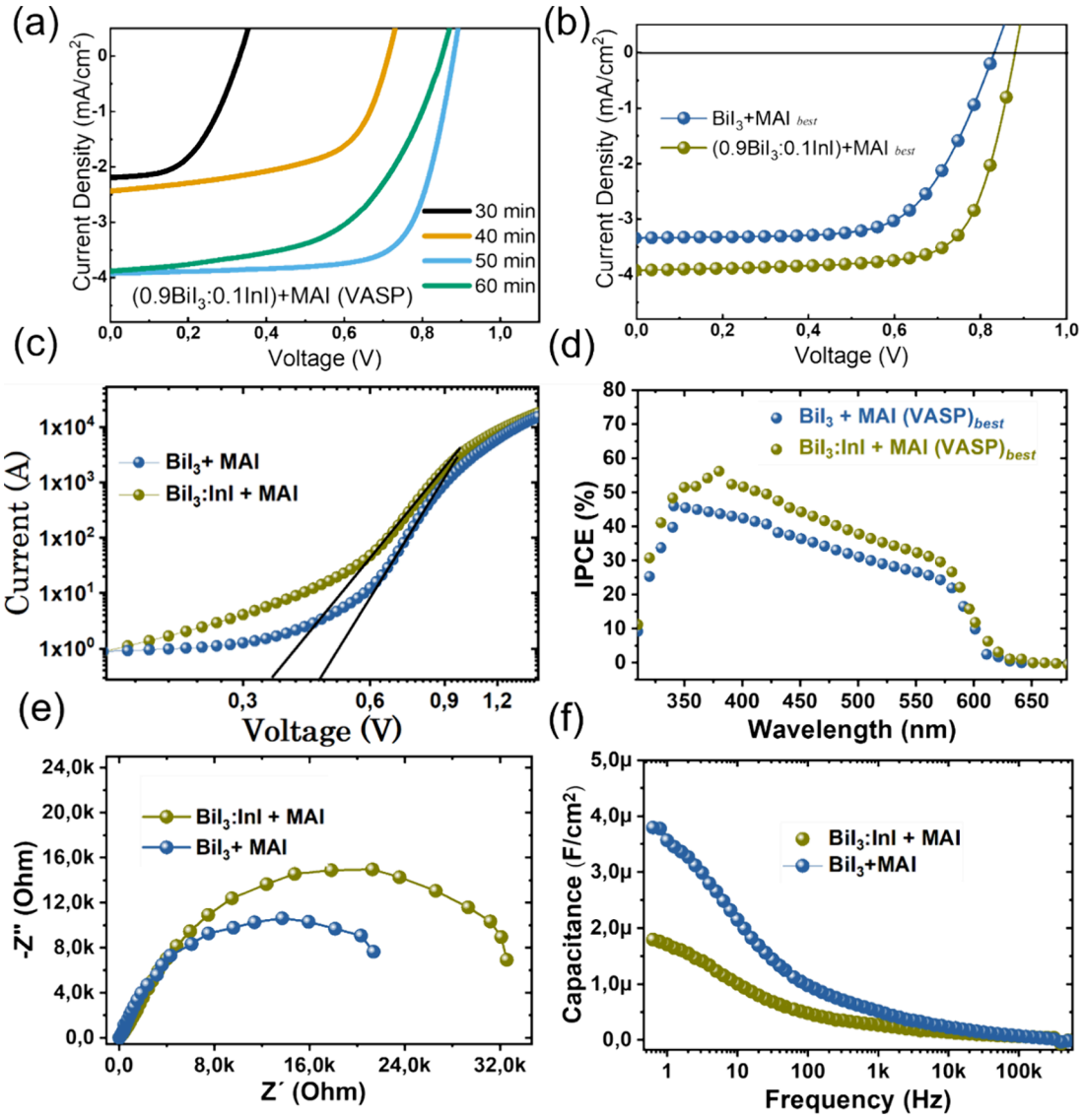

Figure 4. Device performance of all devices. (a) $J-V$ characteristics of different reaction times-based Bi−In devices, and (b) $J-V$ characteristics of both devices under AM 1.5 sunlight. (c) Log−log $I-V$ characteristics of Bi- and Bi−In-based PSCs showing three different regimes. (d) EQE spectra of optimized, champion solar cell devices employing Bi and Bi−In devices. (e) Complex Nyquist plot of Bi and Bi−In devices at 0.2 V in dark conditions. (f) Capacitance-frequency spectra of the devices demonstrate that the low-frequency capacitance (surface polarization) in the Bi−In composition is significantly lower, attributable to the reduced ion migration within the Bi−In lattice.

However, this peak almost disappeared in the In^{3+}-incorporated thin films. This indicates that the In^{3+}-doped Bi-based perovskite thin films are more hydrophobic than pristine thin films. Therefore, In^{3+} incorporation can protect against environmental moisture degradation. The FTIR spectra of BiI_3 and BiI_3:InI_3 spin-coated thin films are given in the Supporting Information (see Figure S9). We also performed contact angle measurements to investigate the hydrophobicity of both absorber layers (Figure S10). Interestingly, the contact angle with water of $(CH_3NH_3)_3Bi_{2-x}In_xI_9$ was increased significantly by 84° compared to $(CH_3NH_3)_3Bi_2I_9$ (61°), proving the moisture resistance of the doped bismuth-based perovskite layers. The Raman spectra of both films exhibited characteristic peaks at the low-wavenumber (50−500 cm^{-1}) and high-wavenumber (500−2200 cm^{-1}) regimes, which are related to the Raman active Bi−I modes of the inorganic framework and the organic MA^+ cation, respectively (see Figure S11). No additional peaks are observed in In^{3+}-doped $(CH_3NH_3)_3Bi_2I_9$ perovskite thin films, suggesting similar crystal structures of both doped and pristine bismuth-based perovskites. Figure 3c,d presents the Raman spectra of BiI_3:InI_3 absorber layers on exposure to MAI(v) for different reaction times. A prominent trend observed from the Raman spectra is the gradual disappearance of the low wavenumber peak with increasing reaction time between MAI(v) and BiI_3:InI, resulting in the weakened Bi−I stretching mode.[39] Since there is no major change in the higher wave peaks, this indicates that the incorporation of In^{3+} with $(CH_3NH_3)_3Bi_2I_9$ has a higher impact on the Bi−I modes of the inorganic framework than on the organic MA^+ cation.

Photovoltaic Performance and Electrical Measurements of Bi-Based PSCs. We have fabricated PSCs with InI_3-doped and pristine MBI perovskite absorber layers using a regular n−i−p structure (FTO/m-TiO_2/perovskite/Spiro-OMeTAD) (Figure S12). The photovoltaic performance of all devices was evaluated by current density−voltage ($J-V$)

https://doi.org/10.1021/acsaelm.4c01576
ACS Appl. Electron. Mater. 2024, 6, 8360−8368

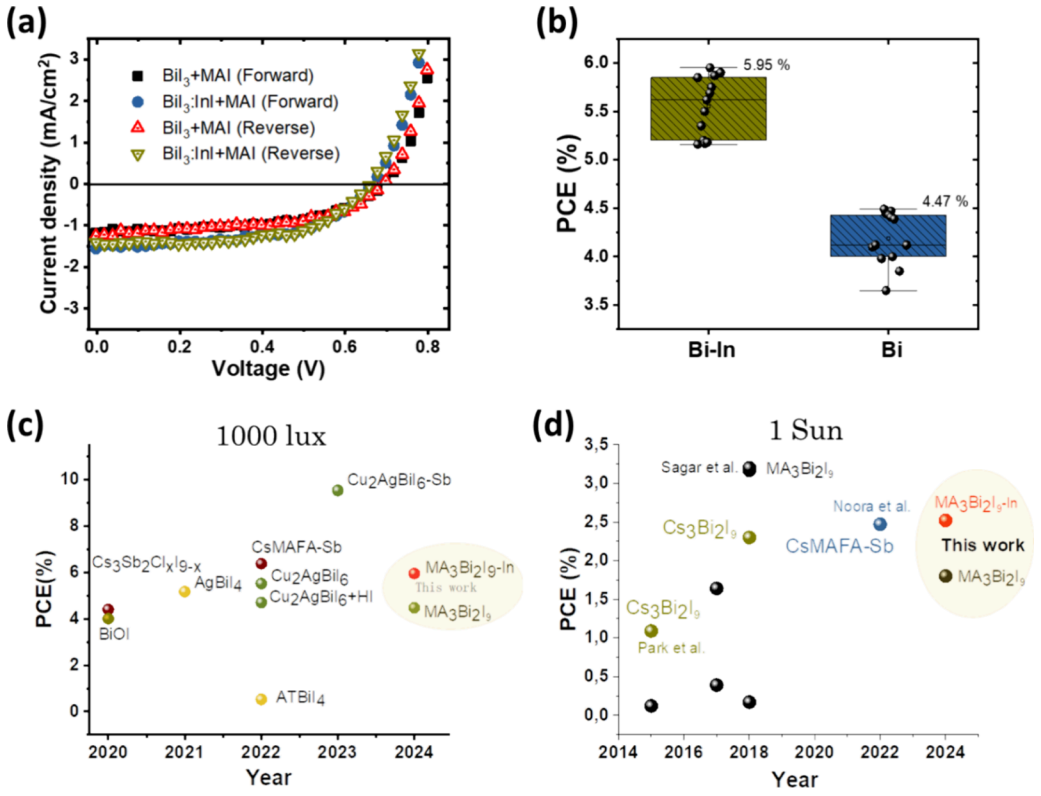

Figure 5. (a) $J-V$ characteristics of champion Bi- and Bi−In-based PSCs under low light intensity of 10 mW/cm^2. (b) Statistical distribution of PCE of both devices at low intensity. The summary of device performance of $A_3B_2X_9$-type Pb-free perovskite solar cells in (c) low light intensity 1000 lx and (d) 1 Sun light intensity.[8,26,34,42]

characteristics under 1 Sun (AM 1.5 G, 100 mW cm^{-2}) (see Figure 4a,b). To demonstrate the importance of mixing bismuth and indium metals at the B-site for maximizing performance, we fabricated a reference cell with pure bismuth at the B-metallic site. Additionally, to illustrate the critical role of reaction time when exposing the BiI_3:InI_3 film to MAI vapor, we fabricated $(CH_3NH_3)_3Bi_{2-x}In_xI_9$ absorbers with varying reaction times, as discussed in previous sections. The device fabrication information is provided in Section 2. The maximum PCE of the reference device without In^{3+} doping is 1.80% with an open-circuit voltage of V_{oc} = 0.83 V, current density J_{sc} = 3.35 mA cm^2, and fill factor FF = 65% for the reaction time of 35 min. However, the bimetallic B-site absorber-based champion device increases V_{oc} to 0.88 V, J_{sc} to 3.92 mA cm^{-2}, FF to 74%, and the overall PCE to 2.55% for 45 min reaction time. The significant enhancement in FF is attributed to the improved surface morphology, leading to reduced nonradiative recombination at interfaces. With increasing reaction time during the exposure of the BiI_3:InI_3 film to MAI vapors, J_{sc} increases and reaches its maximum at 45 min; thereafter, it decreases. This indicates that the crystallization process with the reaction time plays a significant role in charge carrier generation. The device performance parameters of different devices are given in Table S1. The EQE spectrum of BiI_3 + MAI(v) devices prepared with and without In^{3+} shows absorption in the visible spectrum around 625 nm, which is a close match with previously reported Bi-based solar cells (Figure 4d).[8] Interestingly, it is found that the devices prepared with the In^{3+}-doped absorber layer show 10% more absorption as compared to nondoped devices. The highest PCE (2.55%) of $(CH_3NH_3)_3Bi_{2-x}In_xI_9$ is comparable with the previously reported maximum PCE (2.48%) of triple cation-based antimony (CsMAFA-Sb) devices.[34]

Furthermore, we have performed dark current−voltage and electrochemical impedance spectroscopy (EIS) on reference $(CH_3NH_3)_3Bi_2I_9$ (Bi) and bimetallic $(CH_3NH_3)_3Bi_{2-x}In_xI_9$ (Bi−In)-based PSCs to get insight into recombination and ionic kinetics. Figure 4c illustrates the $I-V$ characteristics of both PSCs, showcasing three distinct regimes: a low-voltage regime characterized by current density linearly dependent on applied voltage, dominated by shunt resistance (R_{sh}), termed the Ohmic regime, a mid-voltage regime extending until the built-in voltage (V_{bi}), during which injected charge carriers begin to occupy trap states, referred to as the trap-filled limited (TFL) injection regime. The voltage at which the ohmic and TFL regimes are separated is termed the TFL voltage (V_{TFL}), linearly proportional to trap density.[1] The V_{TFL} of $(CH_3NH_3)_3Bi_2I_9$ is higher than that of $(CH_3NH_3)_3Bi_{2-x}In_xI_9$, revealing the presence of lower trap density in $(CH_3NH_3)_3Bi_{2-x}In_xI_9$-based PSCs.[40,41]

We performed EIS measurements on Bi and Bi−In PSCs at 0.2 V under dark conditions. There are two types of representations, i.e., Nyquist and Bode plots, to analyze the EIS data. Figure 4e shows the complex Nyquist plots of EIS data at 500 mHz to 0.5 MHz at RT. The Nyquist plot exhibits two distinct behaviors: a high-frequency (HF) process and a low-frequency (LF) process. The HF part corresponds to electronic charge transport and bulk recombination, while the LF part is associated with ionic kinetics and interfacial recombinations. The total recombination resistance is determined by combining the high- and low-frequency resistances. Importantly, it should be acknowledged that the

https://doi.org/10.1021/acsaelm.4c01576
ACS Appl. Electron. Mater. 2024, 6, 8360−8368

total recombination resistance can also include a contribution from resistance of the selective contacts; therefore, this is valid only for a qualitative study. It can be noted that the recombination resistance of Bi−In bimetallic PSCs is considerably higher compared to pure Bi-based PSCs, which results in significantly lower recombination in the bimetallic composition and could be attributed to a reduction in bulk defects facilitated by the addition of indium. Additionally, the capacitance-frequency spectra also indicate that bimetallic Bi−In-based PSCs have much lower capacitance at low frequencies (surface polarization) due to reduced ion migration in the bimetallic lattice. This study underscores the significance of incorporating mixed B-site metal cations in lead-free perovskites for the fabrication of efficient Pb-free solar cells tailored for indoor light applications.

We have tested the device performance of Bi- and Bi−In-based PSCs in low light intensity of 10 mW/cm^2. The maximum efficiencies of Bi and Bi−In champion devices are 4.47% and 5.95%, respectively. The statistical distribution of PCE of both devices is shown in Figure 5b. A summary of the device performance of $A_3B_2X_9$-type Pb-free perovskite solar cells in low light intensity and 1 Sun light intensity is reported in Figure 5c,d. It can be noted that the performance of our devices is the highest in bismuth-based PSCs and comparable to antimony-based PSCs.

4. CONCLUSIONS

In conclusion, we incorporated indium iodide into bismuth triiodide for the first time, forming homogeneous precursor films. Subsequent exposure to MAI vapors for varying durations resulted in high-quality lead-free perovskite absorber films for toxic free solar cells. The quality of the films is confirmed by morphological, structural vibrational, optoelectronic characterizations, and EIS. Moreover, the reaction time between BiI_3:InI_3 and MAI vapor plays a crucial role in the vapor-assisted method to fine-tune the optoelectronic properties and morphology of the absorber layer. In^{3+} acts as a passivating agent not only on surface sites but also in bulk absorber material. Furthermore, due to its smaller size relative to Bi^{3+}, In^{3+} does not disrupt the original crystal lattice of the lead-free perovskites. The champion BiI_3:InI_3 + MAI devices with an optimized reaction time of 45 min show a remarkable PCE of 2.55% in 1 Sun and 5.95% in 0.1 Sun. However, the pristine BiI_3+ MAI devices give a maximum PCE of only 1.80% in 1 Sun and 4.47% in 1000 lx illumination. Furthermore, EIS indicates that ion migration is significantly reduced in the bimetallic Bi−In composition compared to the pure Bi-based Pb-free perovskite composition. Overall, this work underscores the significance of reaction time control in the vapor-assisted method and the strategic engineering of B-site metal cations. These approaches are crucial for designing effective Pb-free perovskite photovoltaics for indoor lighting applications.

■ ASSOCIATED CONTENT

Supporting Information

The Supporting Information is available free of charge at https://pubs.acs.org/doi/10.1021/acsaelm.4c01576.

Optical images, FESEM images, XRD pattern, Raman spectra, FTIR spectra, XPS measurements, and contact angle measurements (PDF)

■ AUTHOR INFORMATION

Corresponding Author

Sagar M. Jain − *Center for Renewable and Low Carbon Energy, School of Water, Energy and Environment (SWEE), Cranfield University, Cranfield MK430AL, United Kingdom;* orcid.org/0000-0002-8158-0021; Email: sagar.m.jain@cranfield.ac.uk

Authors

Ramesh Kumar − *Center for Renewable and Low Carbon Energy, School of Water, Energy and Environment (SWEE), Cranfield University, Cranfield MK430AL, United Kingdom; Department of Physics, Indian Institute of Technology Roorkee, Roorkee 247667, India;* orcid.org/0000-0002-7500-8694

Hairui Liu − *College of Material Science and Engineering, Henan Normal University, Xinxiang 453007, China*

Seyed Ali Nabavi − *Center for Renewable and Low Carbon Energy, School of Water, Energy and Environment (SWEE), Cranfield University, Cranfield MK430AL, United Kingdom;* orcid.org/0000-0002-3346-0754

Moses S. Anyebe − *Center for Renewable and Low Carbon Energy, School of Water, Energy and Environment (SWEE), Cranfield University, Cranfield MK430AL, United Kingdom*

Suhas Mahesh − *Department of Physics, University of Oxford, Oxford OX1 3PU, United Kingdom; Department of Electrical and Computer Engineering, University of Toronto, Toronto, Ontario M5S 1A4, Canada;* orcid.org/0000-0002-3897-7963

Henry Snaith − *Department of Physics, University of Oxford, Oxford OX1 3PU, United Kingdom;* orcid.org/0000-0001-8511-790X

Monojit Bag − *Department of Physics, Indian Institute of Technology Roorkee, Roorkee 247667, India*

Complete contact information is available at: https://pubs.acs.org/10.1021/acsaelm.4c01576

Notes

The authors declare no competing financial interest.

■ ACKNOWLEDGMENTS

R.K. is a Commonwealth Scholar, funded by the UK government working in the group of S.M.J. S.M.J. acknowledges commonwealth research funding. M.B. acknowledges the Science and Engineering Research Board (SERB), India, under award no. CRG/2021/001744 dated 07/03/2022 for the partial support to carry out this research work.

■ REFERENCES

(1) Kumar, R.; Srivastava, P.; Bag, M. Role of A-Site Cation and X-Site Halide Interactions in Mixed-Cation Mixed-Halide Perovskites for Determining Anomalously High Ideality Factor and the Super-Linear Power Law in AC Ionic Conductivity at Operating Temperature. *ACS Appl. Electron. Mater.* **2020**, *2* (12), 4087−4098.

(2) Kumar, J.; Kumar, R.; Frohna, K.; Moghe, D.; Stranks, S. D.; Bag, M. Unraveling the Antisolvent Dripping Delay Effect on the Stranski−Krastanov Growth of CH 3 NH 3 PbBr 3 Thin Films: A Facile Route for Preparing a Textured Morphology with Improved Optoelectronic Properties. *Phys. Chem. Chem. Phys.* **2020**, *22* (45), 26592−26604.

(3) Yu, X.; Tsao, H. N.; Zhang, Z.; Gao, P. Miscellaneous and Perspicacious: Hybrid Halide Perovskite Materials Based Photodetectors and Sensors. *Adv. Opt. Mater.* **2020**, *8* (21), No. 2001095.

(4) Mondal, N.; De, A.; Samanta, A. Achieving Near-Unity Photoluminescence Efficiency for Blue-Violet-Emitting Perovskite Nanocrystals. *ACS Energy Lett.* **2019**, *4* (1), 32−39.
(5) Prakasam, V.; Tordera, D.; Di Giacomo, F.; Abbel, R.; Langen, A.; Gelinck, G.; Bolink, H. J. Large Area Perovskite Light-Emitting Diodes by Gas-Assisted Crystallization. *J. Mater. Chem. C* **2019**, *7* (13), 3795−3801.
(6) Berhe, T. A.; Su, W.-N.; Chen, C.-H.; Pan, C.-J.; Cheng, J.-H.; Chen, H.-M.; Tsai, M.-C.; Chen, L.-Y.; Dubale, A. A.; Hwang, B.-J. Organometal Halide Perovskite Solar Cells: Degradation and Stability. *Energy Environ. Sci.* **2016**, *9* (2), 323−356.
(7) Bishop, J. E.; Read, C. D.; Smith, J. A.; Routledge, T. J.; Lidzey, D. G. Fully Spray-Coated Triple-Cation Perovskite Solar Cells. *Sci. Rep.* **2020**, *10* (1), 1−8.
(8) Jain, S. M.; Phuyal, D.; Davies, M. L.; Li, M.; Philippe, B.; De Castro, C.; Qiu, Z.; Kim, J.; Watson, T.; Tsoi, W. C.; Karis, O.; Rensmo, H.; Boschloo, G.; Edvinsson, T.; Durrant, J. R. An Effective Approach of Vapour Assisted Morphological Tailoring for Reducing Metal Defect Sites in Lead-Free, (CH3NH3)3Bi2I9 Bismuth-Based Perovskite Solar Cells for Improved Performance and Long-Term Stability. *Nano Energy* **2018**, *49*, 614−624.
(9) Clark, C. P.; Voigt, B.; Aydil, E. S.; Holmes, R. J. Carrier-Gas Assisted Vapor Deposition for Highly Tunable Morphology of Halide Perovskite Thin Films. *Sustain. Energy Fuels* **2019**, *3* (9), 2447−2455.
(10) Nawaz, A.; Erdinc, A. K.; Gultekin, B.; Tayyib, M.; Zafer, C.; Wang, K.; Akram, M. N.; Wong, K. K.; Hussain, S.; Schmidt-Mende, L.; Fakharuddin, A. Insights into Optoelectronic Properties of Anti-Solvent Treated Perovskite Films. *J. Mater. Sci. Mater. Electron.* **2017**, *28* (20), 15630−15636.
(11) Amgar, D.; Aharon, S.; Etgar, L. Inorganic and Hybrid Organo-Metal Perovskite Nanostructures: Synthesis, Properties, and Applications. *Adv. Funct. Mater.* **2016**, *26* (47), 8576−8593.
(12) Srivastava, P.; Kumar, R.; Bag, M. Discerning the Role of an A-Site Cation and X-Site Anion for Ion Conductivity Tuning in Hybrid Perovskites by Photoelectrochemical Impedance Spectroscopy. *J. Phys. Chem. C* **2021**, *125* (1), 211−222.
(13) Sun, Y.; Peng, J.; Chen, Y.; Yao, Y.; Liang, Z. Triple-Cation Mixed-Halide Perovskites: Towards Efficient, Annealing-Free and Air-Stable Solar Cells Enabled by Pb(SCN) 2 Additive OPEN. *Nat. Publ. Gr.* **2017**.
(14) *Best Research-Cell Efficiency Chart*. https://www.nrel.gov/pv/cell-efficiency.html (accessed 2021−01−25).
(15) Hakamata, T.; Shimamura, K.; Shimojo, F.; Kalia, R. K.; Nakano, A.; Vashishta, P. The Nature of Free-Carrier Transport in Organometal Halide Perovskites. *Sci. Rep.* **2016**, *6*, 19599.
(16) Wu, X.; Xie, L.; Lin, K.; Lu, J.; Wang, K.; Feng, W.; Fan, B.; Yin, P.; Wei, Z. Efficient and Stable Carbon-Based Perovskite Solar Cells Enabled by the Inorganic Interface of CuSCN and Carbon Nanotubes. *J. Mater. Chem. A* **2019**, *7* (19), 12236−12243.
(17) Wang, K.; Jin, L.; Gao, Y.; Liang, A.; Finkenauer, B. P.; Zhao, W.; Wei, Z.; Zhu, C.; Guo, T.-F.; Huang, L.; Dou, L. Lead-Free Organic-Perovskite Hybrid Quantum Wells for Highly Stable Light-Emitting Diodes. *ACS Nano* **2021**, *15*, 6316.
(18) Hwang, B.; Lee, J. S. Lead-Free, Air-Stable Hybrid Organic-Inorganic Perovskite Resistive Switching Memory with Ultrafast Switching and Multilevel Data Storage. *Nanoscale* **2018**, *10* (18), 8578−8584.
(19) Zuo, C.; Ding, L. Lead-Free Perovskite Materials (NH4)-3Sb2IxBr9−x. *Angew. Chemie - Int. Ed.* **2017**, *56* (23), 6528−6532.
(20) De Angelis, F. The Prospect of Lead-Free Perovskite Photovoltaics. *ACS Energy Lett.* **2021**, *6* (4), 1586−1587.
(21) Liu, X.; Wu, T.; Luo, X.; Wang, H.; Furue, M.; Bessho, T.; Zhang, Y.; Nakazaki, J.; Segawa, H.; Han, L. Lead-Free Perovskite Solar Cells with Over 10% Efficiency and Size 1 cm2 Enabled by Solvent−Crystallization Regulation in a Two-Step Deposition Method. *ACS Energy Lett.* **2022**, *7* (1), 425−431.
(22) Cao, J.; Yan, F. Recent Progress in Tin-Based Perovskite Solar Cells. *Energy and Environmental Science.* **2021**, *14*, 1286−1325.
(23) Zhang, M.; Zhang, Z.; Cao, H.; Zhang, T.; Yu, H.; Du, J.; Shen, Y.; Zhang, X. L.; Zhu, J.; Chen, P.; Wang, M. Recent Progress in Inorganic Tin Perovskite Solar Cells. *Materials Today Energy.* **2022**, *23*, No. 100891.
(24) Mahmoudi, T.; Rho, W. Y.; Kohan, M.; Im, Y. H.; Mathur, S.; Hahn, Y. B. Suppression of Sn2+/Sn4+ Oxidation in Tin-Based Perovskite Solar Cells with Graphene-Tin Quantum Dots Composites in Active Layer. *Nano Energy* **2021**, *90*, No. 106495.
(25) Jin, Z.; Zhang, Z.; Xiu, J.; Song, H.; Gatti, T.; He, Z. A Critical Review on Bismuth and Antimony Halide Based Perovskites and Their Derivatives for Photovoltaic Applications: Recent Advances and Challenges. *J. Mater. Chem. A* **2020**, *8* (32), 16166−16188.
(26) Jain, S. M.; Edvinsson, T.; Durrant, J. R. Green Fabrication of Stable Lead-Free Bismuth Based Perovskite Solar Cells Using a Non-Toxic Solvent. *Commun. Chem. 2019 21* **2019**, *2* (1), 1−7.
(27) Tewari, N.; Shivarudraiah, S. B.; Halpert, J. E. Photo-rechargeable Lead-Free Perovskite Lithium-Ion Batteries Using Hexagonal Cs3Bi2I9Nanosheets. *Nano Lett.* **2021**, *21* (13), 5578−5585.
(28) Ahmad, K. Bismuth Halide Perovskites for Photovoltaic Applications. In *Bismuth - Fundamentals and Optoelectronic Applications*; IntechOpen, 2020. .
(29) Jia, Q.; Li, C.; Tian, W.; Johansson, M. B.; Johansson, E. M. J.; Yang, R. Large-Grained All-Inorganic Bismuth-Based Perovskites with Narrow Band Gap via Lewis Acid−base Adduct Approach. *ACS Appl. Mater. Interfaces* **2020**, *12* (39), 43876−43884.
(30) Hu, W.; He, X.; Fang, Z.; Lian, W.; Shang, Y.; Li, X.; Zhou, W.; Zhang, M.; Chen, T.; Lu, Y.; Zhang, L.; Ding, L.; Yang, S. Bulk Heterojunction Gifts Bismuth-Based Lead-Free Perovskite Solar Cells with Record Efficiency. *Nano Energy* **2020**, *68*, No. 104362.
(31) Banerjee, P.; Kumar, N. S.; Naidu, K. C. B.; Franco, A.; Dachepalli, R. Stability of 2D and 3D Perovskites Due to Inhibition of Light-Induced Decomposition. *J. Electron. Mater.* **2020**, *49* (12), 7072−7084.
(32) Tang, M. C.; Barrit, D.; Munir, R.; Li, R.; Barbé, J. M.; Smilgies, D. M.; Del Gobbo, S.; Anthopoulos, T. D.; Amassian, A. Bismuth-Based Perovskite-Inspired Solar Cells: In Situ Diagnostics Reveal Similarities and Differences in the Film Formation of Bismuth- and Lead-Based Films. *Sol. RRL* **2019**, *3* (7), No. 1800305.
(33) Park, B.-W.; Philippe, B.; Zhang, X.; Rensmo, H.; Boschloo, G.; Johansson, E. M. J. Bismuth Based Hybrid Perovskites A3Bi2 I9 (A: Methylammonium or Cesium) for Solar Cell Application. *Adv. Mater.* **2015**, *27* (43), 6806−6813.
(34) Lamminen, N.; Grandhi, G. K.; Fasulo, F.; Hiltunen, A.; Pasanen, H.; Liu, M.; Al-Anesi, B.; Efimov, A.; Ali-Löytty, H.; Lahtonen, K.; Mäkinen, P.; Matuhina, A.; Muñoz-García, A. B.; Pavone, M.; Vivo, P. Triple A-Site Cation Mixing in 2D Perovskite-Inspired Antimony Halide Absorbers for Efficient Indoor Photovoltaics. *Adv. Energy Mater.* **2023**, *13* (4), No. 2203175.
(35) Tavakoli, M. M.; Fazel, Z.; Tavakoli, R.; Akin, S.; Satapathi, S.; Prochowicz, D.; Yadav, P. Efficient and Less-Toxic Indium-Doped MAPbI3 Perovskite Solar Cells Prepared by Metal Alloying Technique. *Sol. RRL* **2022**, *6*, No. 2200106.
(36) Kumar, R.; Shukla, P. S.; Varma, G. D.; Bag, M. Synthesis of Porous Electrode from CH3NH3PbBr3 Single Crystal for Efficient Supercapacitor Application: Role of Morphology on the Charge Storage and Stability. *Electrochim. Acta* **2021**, *398*, No. 139344.
(37) Li, C.; Hu, J.; Wang, S.; Ren, J.; Chen, B.; Pan, T.; Niu, X.; Hao, F. Lattice Strain Relaxation and Grain Homogenization for Efficient Inverted MAPbI3 Perovskite Solar Cells. *J. Phys. Chem. Lett.* **2021**, *12* (19), 4569−4575.
(38) Zou, Y.; Eichhorn, J.; Zhang, J.; Apfelbeck, F. A. C.; Yin, S.; Wolz, L.; Chen, C. C.; Sharp, I. D.; Müller-Buschbaum, P. Microstrain and Crystal Orientation Variation within Naked Triple-Cation Mixed Halide Perovskites under Heat, UV, and Visible Light Exposure. *ACS Energy Lett.* **2024**, *9* (2), 388−399.
(39) Gu, J.; Yan, G.; Lian, Y.; Mu, Q.; Jin, H.; Zhang, Z.; Deng, Z.; Peng, Y. Bandgap Engineering of a Lead-Free Defect Perovskite

Cs3Bi2I9 through Trivalent Doping of Ru3+. *RSC Adv.* **2018**, *8* (45), 25802−25807.
(40) Kumar, R.; Kumar, J.; Srivastava, P.; Moghe, D.; Kabra, D.; Bag, M. Unveiling the Morphology Effect on the Negative Capacitance and Large Ideality Factor in Perovskite Light-Emitting Diodes. *ACS Appl. Mater. Interfaces* **2020**, *12* (30), 34265−34273.
(41) Saidaminov, M. I.; Abdelhady, A. L.; Murali, B.; Alarousu, E.; Burlakov, V. M.; Peng, W.; Dursun, I.; Wang, L.; He, Y.; MacUlan, G.; Goriely, A.; Wu, T.; Mohammed, O. F.; Bakr, O. M. High-Quality Bulk Hybrid Perovskite Single Crystals within Minutes by Inverse Temperature Crystallization. *Nat. Commun.* **2015**, *6*, 7586.
(42) Pious, J. K.; Lekshmi, M. L.; Muthu, C.; Rakhi, R. B.; Nair, V. C. Zero-Dimensional Methylammonium Bismuth Iodide-Based Lead-Free Perovskite Capacitor. *ACS Omega* **2017**, *2*, 5798−5802.

https://doi.org/10.1021/acsaelm.4c01576
ACS Appl. Electron. Mater. 2024, 6, 8360−8368